American Mineralogist, Volume 91, pages 1893–1900, 2006

Single-crystal elasticity of brucite, $Mg(OH)_2$, to 15 GPa by Brillouin scattering

FUMING JIANG,* SERGIO SPEZIALE,† AND THOMAS S. DUFFY

Department of Geosciences, Princeton University, Princeton, New Jersey 08544, U.S.A.

ABSTRACT

The second-order elastic constants of brucite were determined by Brillouin scattering to 15 GPa in a diamond anvil cell. The experiments were carried out using a 4:1 methanol-ethanol mixture as pressure medium, and ruby as a pressure standard. Two planes, one perpendicular to the *c* axis (basal plane) and the other containing the *c* axis (meridian plane), were measured at room pressure and 10 elevated pressures. Individual elastic stiffnesses, aggregate moduli, and their pressure derivatives were obtained by fitting the data to Eulerian finite strain equations. The inversion yields individual elastic constants of C_{11} = 154.0(14) GPa, C_{33} = 49.7(7) GPa, C_{12} = 42.1(17) GPa, C_{13} = 7.8(25) GPa, C_{14} = 1.3(10) GPa, C_{44} = 21.3(4) GPa, and their pressure derivatives of $(\partial C_{11}/\partial P)_0$ = 9.0(2), $(\partial C_{33}/\partial P)_0$ = 14.0(5), $(\partial C_{12}/\partial P)_0$ = 3.2(2), $(\partial C_{13}/\partial P)_0$ = 5.0(1), $(\partial C_{14}/\partial P)_0$ = 0.9(1), $(\partial C_{44}/\partial P)_0$ = 3.9(1). Aggregate moduli and their pressure derivatives are K_{S0} = 36.4(9) GPa, G_0 = 31.3(2) GPa, $(\partial K_S/\partial P)_{T0}$ = 8.9(4), $(\partial G/\partial P)_0$ = 4.3(1) for the Reuss bound, and K_{S0} = 43.8(8) GPa, G_0 = 35.2(3) GPa, $(\partial K_S/\partial P)_{T0}$ = 6.8(2), $(\partial G/P)_0$ = 3.4(1) for the Voigt-Reuss-Hill average. The ratio of the linear compressibility along the *c* and *a* axes decreased from 4.7 to 1.3 over the examined pressure range. The shear anisotropy (C_{66}/C_{44}) decreased from 2.6(1) at ambient condition to 1.3(1) with increase of pressure to 12 GPa. Axial compressibilities and a compression curve constructed from our Brillouin data are in good agreement with previous X-ray diffraction data. The increased interlayer interactions and hydrogen repulsion that occurs as brucite is compressed produce a continuous variation of elastic properties rather than any abrupt discontinuities.

Keywords: Brucite, elasticity, high pressure, brillouin scattering

INTRODUCTION

The high-pressure behavior of brucite-type hydroxides has been extensively examined in recent years as a model system for understanding hydrous minerals under compression. Brucite, $Mg(OH)_2$, has a simple layered structure in which each Mg ion is surrounded by a distorted octahedron of O atoms. The Mg ions lie in planes with the O ions above and below them in a sandwich arrangement. The O-H bonds are perpendicular to these planes. The octahedral sheets are stacked along the *c*-direction with weak interlayer bonding.

Geologically, brucite is found in serpentinites (Hostetler et al. 1966), and is expected to be an important phase in the forearc mantle overlying subduction zones, forming as a result of reaction between infiltrating fluids and the ultramafic mantle (Peacock and Hyndman 1999). Many phyllosilicates such as lizardite and talc include brucite-like layers as one of their principal structural units. The brucite dehydration reaction has also long been used to study volumetric properties of H_2O at elevated pressures and temperatures (Irving et al. 1977; Johnson and Walker 1993; Mirwald 2005; Fukui et al. 2005). High-pressure studies have revealed a varied range of phenomena in brucite-type hydroxides including pressure-induced amorphization, sublattice amorphization, crystal structure changes, hydrogen repulsion, and structural frustration (Kruger et al. 1989; Meade and Jeanloz 1990; Parise et al. 1994; Catti et al. 1995; Duffy et al. 1991, 1995a; Kunz et al. 1996; Raugei et al. 1999; Shieh and Duffy 2002; Shinoda et al. 2002; Mookherjee and Stixrude 2005; Speziale et al. 2005; Shim et al. 2006).

Neutron diffraction studies of $Mg(OD)_2$ indicate that the deuteriums move to three off-axis sites in response to deuterium-deuterium repulsion induced by compression (Parise et al. 1994). The high-pressure behavior of brucite has also been studied by shock techniques (Duffy et al. 1991) and by theoretical calculations using density functional theory (Raugei et al. 1999; Mookherjee and Stixrude 2005). Static compression studies of brucite indicate that initially the compressibility is much greater normal to layering than parallel to it (Fei and Mao 1993; Duffy et al. 1995b). Brillouin scattering measurements at ambient pressure show that the elastic constant C_{11} is about three times larger than C_{33} (Xia et al. 1998). The relative axial compressibilities change drastically over modest pressures with the *c*/*a* ratio initially decreasing before becoming nearly pressure independent by 15 GPa (Fei and Mao 1993; Catti et al. 1995; Duffy et al. 1995a; Nagai et al. 2000). To better understand the mechanical response of brucite to hydrostatic compression, we have determined the complete elastic tensor of brucite to 15 GPa using Brillouin scattering in the diamond anvil cell.

EXPERIMENTAL METHODS

Crystals with dimensions of approximately 30 × 30 × 15 mm were taken from natural brucite samples. The composition of the crystals was determined by electron microprobe analysis (Table 1). Six points were analyzed across each of two selected crystals and the average composition was $Mg_{0.98}Mn_{0.02}(OH)_2$. Powder

* E-mail: fumingj@princeton.edu

† Present address: GeoForschungsZentrum Potsdam, Division 4.1, Telegrafenberg, 14473 Potsdam, Germany.

0003-004X/06/1112–1893$05.00/DOI: 10.2138/am.2006.2215

X-ray diffraction patterns obtained at X17C of the National Synchrotron Light Source matched very well with expected peak positions for brucite and yielded lattice parameters of $a = 3.150(1)$ Å and $c = 4.783(5)$ Å. Individual crystals show a tabular habit and cleave easily on {0001} to form thin basal-plane sheets. Special attention was paid to the sample preparation because brucite is soft and cleaves easily under stress.

For the basal plane, a natural cleavage platelet was used without further preparation for both room pressure and high-pressure Brillouin measurements. To obtain a platelet containing the [001]-axis (hereafter referred to as the meridian plane), a brucite piece with dimensions $15 \times 10 \times 6$ mm was placed vertically and immersed in epoxy in a cylindrical container with a diameter of 25 mm. After the epoxy solidified, the cylinder was cut into a disk with a thickness of 5 mm. The disk was then double-side polished with successively finer grits down to a final alumina paper of 1 µm. To prevent distortion or bending of the brucite crystal, it was kept in the epoxy disk and had a final size of $15 \times 3 \times 3$ mm. The meridian platelet was first measured at room pressure and then further polished to a thickness of 30 µm for high-pressure measurement. The basal and the meridian platelets, each with approximate thickness of 30 µm and lateral dimensions of 100×100 µm, were loaded separately into modified Merrill-Basset diamond anvil cells with angular opening of 96°. Stainless steel gaskets were pre-indented to 50–60 µm and then a 250 µm diameter hole was drilled in the center of the anvil indentation. A 4:1 methanol-ethanol mixture was used as pressure transmitting medium, and more than four ruby chips were placed around the sample as pressure standards. Both samples were compressed to about 15 GPa with 10 individual pressure steps. Pressure was determined by measuring the ruby fluorescence shift (Mao et al. 1986). The fluorescence peaks did not show significant broadening over the examined pressure range. To allow for possible stress relaxation after each compression step, Brillouin measurements were carried out at least one day after pressure increase. The differences between pressures measured from different ruby chips around the samples never exceeded ±0.2 GPa except for the last pressure near 14.6 ± 0.5 GPa. Pressures measured before and after each Brillouin data set collection were always equivalent within mutual uncertainties.

The samples were excited with a single frequency vertically polarized neodymium vanadate laser ($\lambda = 532.15$ nm) with a power of 150 mW. Brillouin spectra were measured using a six-pass Sandercock tandem Fabry-Perot interferometer in a forward symmetric scattering geometry in which acoustic velocities, V, can be determined without knowledge of the sample refractive index (Whitfield et al. 1976):

$$V = \frac{\nu_B \lambda_0}{2\sin(\theta/2)} \quad (1)$$

where, λ_0 is the incident laser wavelength, $\Delta\nu_B$ is the measured Brillouin frequency shift and θ is the scattering angle external to the diamond cell (70 ± 0.03° in this study). For both planes, Brillouin spectra were recorded in more than 37 directions over an angular range of 180° with 5° steps. Typical spectrum collection time is between 4 to 10 minutes. Eulerian angles (θ_0, $\phi_0+\phi$, χ_0) relating the crystallographic coordinate system to the laboratory coordinate system were used to specify the crystal orientation and acoustic wave-vector direction (Shimizu 2004). The azimuthal angle, ϕ, was the only one that was varied during measurement. The accuracy, precision, and reproducibility of our system were tested on standard single crystals of MgO and $SrTiO_3$ with known velocities and we reproduced the expected velocities with an uncertainty less than 0.5%. Details of the experimental setup are reported elsewhere (Speziale and Duffy 2002; Jiang et al. 2004a, 2004b).

RESULTS

Figure 1 shows typical Brillouin spectra at 1 bar and 7.5 GPa for the basal and meridian plane. The measured frequency shifts have been converted to velocity along the horizontal axis using Equation 1. For the basal plane, all three acoustic modes, one quasi-longitudinal (LA) and two quasi-transverse (TA1 and TA2) acoustic modes were observed. While for the meridian plane, one LA mode and one TA mode were observed below 8.8 GPa. Above 8.8 GPa, both TA1 and TA2 modes were observed at some angles, and this helps in the TA mode assignment of the two TA branches.

Brucite crystallizes in the trigonal system ($P\bar{3}m1$) and is characterized by 6 independent elastic stiffness constants (C_{11}, C_{33}, C_{12}, C_{13}, C_{14}, and C_{44}). The velocity data for all modes in both planes at each pressure were fit together using non-linear least squares methods to Christoffel's equation (Every 1980) to retrieve the six elastic constants and six Eulerian angles describing the two crystal orientations. The procedure for the acoustic mode assignment and inversion for the elastic constants has been reported elsewhere (Speziale and Duffy 2002; Jiang et al. 2004a, 2004b). A starting model based on literature values of C_{ij} (Xia et al. 1998) and density at ambient conditions was used for the room-pressure velocity fitting, and the initial Eulerian angles for (θ_0, ϕ_0, χ_0) were systematically varied until a satisfactory agreement between calculated and experimentally obtained velocities was attained. Elastic constants and orientations were then further refined by non-linear least squares. Densities at high pressures were initially estimated by using the Birch-Murnaghan equation of state, with ambient pressure values of the isothermal bulk modulus, K_{T0}, and an initial guess for the pressure derivative of the isothermal bulk modulus, $K'_{T0} = (\partial K_T/\partial P)_{T0}$. High-pressure elastic constants were obtained by fitting the velocity curves using the calculated density and the C_{ij} values from the previous pressure as initial guesses. A ±0.1 GPa uncertainty of pressure was propagated in our density error when estimating the errors in elastic moduli.

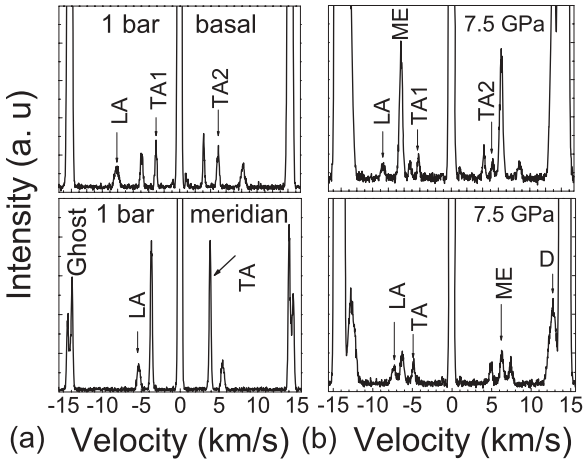

FIGURE 1. Brillouin spectra at (**a**) 1 bar and (**b**) 7.5 GPa. Upper and lower panels are for the basal plane and meridian plane, respectively. LA = longitudinal acoustic mode; TA = transverse acoustic mode; TA1 and TA2 are the slow and fast TA mode, respectively. D = diamond TA mode; ME = methanol-ethanol medium.

TABLE 1. Result of microprobe and powder X-ray diffraction analysis at ambient conditions

Oxides (wt%) Sample	MgO	Al_2O_3	SiO_2	CaO	MnO	FeO	Na_2O	H_2O	SUM
No. 1	65.780	0.003	0.019	0.050	0.781	0.007	0.030	31.052	97.700
No. 2	64.458	0.000	0.020	0.081	2.236	0.005	0.020	30.824	97.700

Notes: Average Composition: $Mg_{0.982}Mn_{0.018}(OH)_2$; Lattice Parameters: $a = 3.150(1)$ Å, $c = 4.783(5)$ Å; Density: $\rho = 2.379(4)$ g/cm³.

After the first round of fitting, the full compliance tensor (S_{ij}) was calculated from the elastic stiffness tensor (C_{ij}) at each pressure. Adiabatic aggregate bulk, K_S, and shear moduli, G, in the Reuss (isostress) limit were then calculated (Watt et al. 1976). The Reuss bound to the aggregate bulk modulus was fit to the third-order Eulerian finite strain equation (Birch 1978) to obtain K_{S0} and $K'_{S0} = (\partial K_S/\partial P)_{T0}$. These parameters were then converted to isothermal values, K_{T0} and $(\partial K_T/\partial P)_{T0}$, by applying the thermodynamic relations:

$$K_{T0} = K_{S0}/(1 + \alpha\gamma T) \quad (2)$$

$$(\partial K_T / \partial P)_{T0} \approx (1+\alpha\gamma T)^{-1}[(\partial K_S / \partial P)_{T0} - \gamma T / K_{T0}(\partial K_T / \partial T)_{P0}] \quad (3)$$

where α is the volume thermal expansion coefficient and γ is the Gruneisen parameter (Table 2). We note that there has been some variability in the γ values reported in the literature (Duffy et al. 1991; Redfern and Wood 1992). The isothermal K_{T0} and K'_{T0} were then used to construct improved isothermal compression curves and to refine densities at high pressures. The velocities at each pressure were refit using refined densities. The above procedure was repeated until convergence was achieved after four iterations.

Figures 2 and 3 show the observed velocities (symbols) and calculated velocity curves (lines) of brucite for the meridian plane and the basal plane at room pressure and a pressure of 10.8 GPa. Table 3 displays the best-fit density, elastic constants, and the root mean square (RMS) differences between observed and calculated velocities at all pressures. The fit was very good, as reflected in the low RMS deviations (Table 3). The variation of the elastic constants as a function of pressure is shown in Figure 4. The ambient-pressure elastic constants and pressure derivatives obtained from fitting to Eulerian finite strain equations are shown in Table 4.

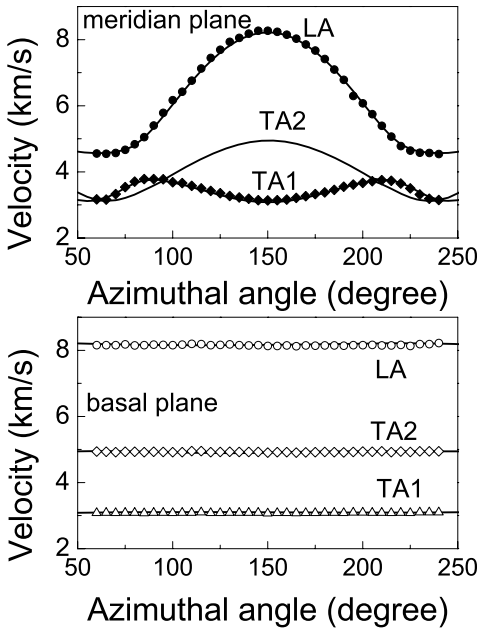

FIGURE 2. Velocity data at 1 bar for the meridian plane (upper) and the basal plane (lower); symbols are observed velocities; solid lines are calculated from best-fitting elastic constants.

DISCUSSION

Elastic stiffness constants, aggregate moduli, and pressure derivatives

Our observed C_{ij} are generally in good agreement with those obtained by previous Brillouin measurements (Xia et al. 1998) within uncertainties (Table 4, Fig. 4). However, the measured C_{11} and C_{13} are slightly higher than the fit values at room pressure. This may be due either to small amounts of strain in the room-pressure brucite sample and/or the uncertainties in assigning the TA modes for the meridian plane. It was found in our experiment that brucite tends to bend and cleaves easily during polishing when the sample becomes thin. Therefore the meridian platelet of brucite was measured at room pressure with the sample fixed in an epoxy disk. The sample was removed from the epoxy after further thinning for the high-pressure measurements. This may cause slight differences for certain constants due to strain differences. Another uncertainty is caused by TA mode assignment for the meridian plane. As seen from Figure 1, only one TA mode was observed for the meridian platelet at room-pressure. In the present study, a trial and error method was used in the TA mode assignment (Speziale and Duffy 2002; Jiang et al. 2004a, 2004b) until a satisfactory agreement was obtained between cal-

TABLE 2. Thermodynamic parameters used for adiabatic to isothermal conversion

Parameter	Value	References
Density ρ_0	2.38 g/cm³	This study
Thermal expansion α_0	5.0×10^{-5} K^{-1}	Xia et al. (1998)
Grüneisen parameter γ_0	0.58	Calculated*
Specific heat C_P	76.62 J/(mol·K)	Berman and Brown (1985)
$(\partial K_{T0}/\partial T)_{P0}$	–0.011 GPa/K	Xia et al. (1998)

* Grüneisen parameter obtained as $\gamma_0 = \alpha_0 K_{0,V}/(\rho_0 C_P)$.

TABLE 3. Best-fit density, elastic constants

P (GPa)	ρ (g/cm³)	C_{11} (GPa)	C_{33} (GPa)	C_{12} (GPa)	C_{13} (GPa)	C_{44} (GPa)	C_{14} (GPa)	RMS (m/s)
10^{-4}	2.38	159.0(16)	49.5(7)	43.3(17)	11.1(25)	22.8(4)	1.8(25)	31
1.1(1)	2.446	164.1(10)	59.2(7)	45.5(8)	12.3(8)	25.2(3)	3.1(4)	50
2.1(1)	2.496	169.3(9)	73.2(7)	46.2(8)	16.6(7)	28.9(3)	4.1(4)	43
3.5(1)	2.558	179.6(10)	94.0(8)	52.0(9)	22.1(8)	33.4(3)	4.8(5)	48
4.8(1)	2.605	184.3(8)	110.0(6)	53.1(6)	28.2(5)	36.8(3)	5.6(3)	30
6.1(1)	2.650	191.7(8)	125.7(7)	57.4(6)	33.9(6)	40.7(3)	7.2(4)	33
7.5(1)	2.693	202.0(9)	141.2(9)	61.0(10)	39.5(9)	44.5(3)	7.9(5)	51
8.8(1)	2.731	209.0(8)	155.6(8)	63.4(8)	44.9(7)	48.9(3)	10.1(4)	41
10.8(1)	2.783	221.3(8)	173.7(9)	70.6(9)	52.1(7)	54.4(4)	12.2(4)	41
12.4(2)	2.823	228.1(7)	182.1(9)	70.4(8)	55.9(7)	58.8(4)	13.3(4)	35
14.6(5)	2.873	239.9(12)	201.9(18)	71.6(16)	68.0(14)	66.3(7)	15.1(6)	74

Notes: RMS = root mean square of the difference between observed and calculated sound velocities. Numbers in parenthesis are 1-σ deviations in last digits.

TABLE 4. Extrapolated individual elastic constants, and their pressure derivatives at ambient conditions

Elastic constants	C_{11} (GPa)	C_{33} (GPa)	C_{12} (GPa)	C_{13} (GPa)	C_{14} (GPa)	C_{44} (GPa)
$Mg(OH)_2$						
This study*	154.0(14)	49.7(7)	42.1(17)	7.8(25)	1.3(10)	21.3(4)
This study†	159.0(16)	49.5(7)	43.3(17)	11.1(25)	1.8(25)	22.8(4)
Xia et al.(1998)	156.7(8)	46.3(8)	44.4(10)	12.0(15)	0.2(8)	21.7(5)
Pressure derivatives						
	$\partial C_{11}/\partial P$	$\partial C_{33}/\partial P$	$\partial C_{12}/\partial P$	$\partial C_{13}/\partial P$	$\partial C_{14}/\partial P$	$\partial C_{44}/\partial P$
This study	9.0(2)	14.0(5)	3.2(2)	5.0(1)	0.9(1)	3.9(1)

* From fit to Eulerian finite strain equations.
† Observed values.

culated, and measured velocities and orientations were reached. For pressures above 8.8 GPa, two TA modes appeared at some angles for the meridian platelet, and this greatly reduced the uncertainty in TA mode assignment both above and below 8.8 GPa and constrained the crystal orientation much better. Larger 1-σ standard deviations are given at room pressure in Table 3 due to the uncertainty in mode assignment and poorer constraint of crystal orientation for the meridian platelet.

Using the measured elastic constants, the Reuss and Voigt bounds, and Voigt-Reuss-Hill (VRH) average of the aggregate bulk and shear moduli were calculated and fit to the Eulerian finite strain equations (Table 5). Figure 5 shows the pressure dependencies of the aggregate moduli: filled symbols are from the present study, lines are fits, and open symbols are from the literature (Xia et al. 1998). The Reuss bound on the isothermal bulk modulus and its pressure derivative is compared with literature values (mainly static compression) in Table 6. The present study is the first high-pressure measurement to obtain all individual elastic constants, bulk moduli, and their pressure derivatives.

There are several interesting features of the elasticity of brucite aggregates as a function of pressure. First, there is a large difference between the Voigt and Reuss bounds on the aggregate moduli, with differences of 40% for the bulk modulus and 25% for the shear modulus. However, these differences, which reflect the degree of elastic anisotropy (Chung and Buessem 1972), decrease rapidly with pressure, and at the highest pressure, the difference in bounds for the bulk and shear moduli are only about 1 and 3%, respectively. Other aggregate elastic constants show a strong variation with pressure. The aggregate Poisson's ratio is given by $\sigma = (3K - 2G)/[2(3K + G)]$, where K is the bulk modulus and G is the aggregate shear modulus. Using the Reuss

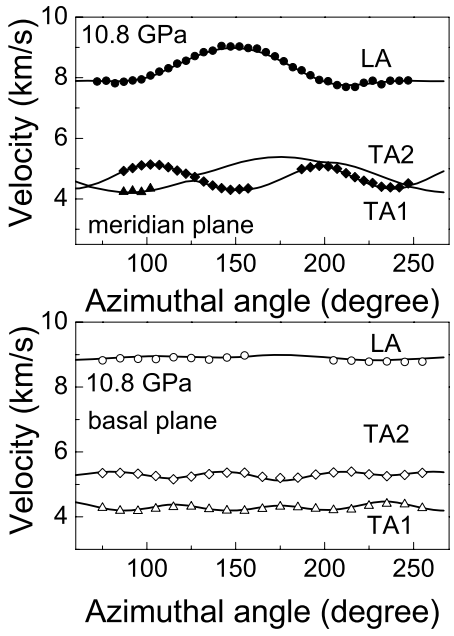

FIGURE 3. Velocity data at 10 GPa for the meridian plane (upper) and the basal plane (lower); symbols are observed velocities; solid lines are calculated from best-fitting elastic constants.

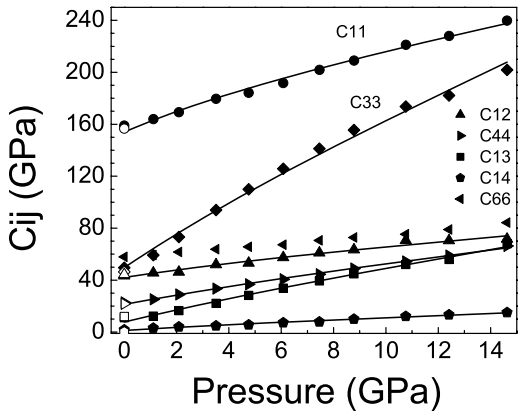

FIGURE 4. Pressure dependencies of the elastic stiffness constants C_{ij}; C_{66} is given by $(C_{11} - C_{12})/2$; solid lines are fits using Eulerian finite strain equations; open symbols are from Xia et al. (1998.)

TABLE 5. Aggregate moduli and pressure derivatives at ambient conditions

This study	Reuss	Voigt	VRH
K_{0S} (GPa)	36.4(9)	51.2(10)	43.8(8)
K_{0T} (GPa)	35.8(9)	50.5(10)	43.2(8)
G_0 (GPa)	31.3(2)	39.1(5)	35.2(3)
$\partial K_{0S}/\partial P$	8.9(4)	5.2(2)	6.8(2)
$\partial K_{0T}/\partial P$	8.9(4)	5.2(2)	6.8(2)
$\partial G_0/\partial P$	4.3(1)	2.7(1)	3.4(1)

TABLE 6. Bulk moduli (Reuss) and their pressure derivatives of brucite at 300 K

References	K_{0T} (GPa)	$(\partial K_T/\partial P)_0$	Method
Duffy et al. (1991)	51(4)	5.0(4)	SW
Fei and Mao (1993)	54.3	4.7	PXD
Parise et al. (1994)	47	4.7*	PND
Duffy et al. (1995)	42	5.7	SCXD
Catti et al. (1995)	39	7.6	PND
Nagai et al. (2000)	44	6.7*	PXD
Fukui et al. (2003)	41.8(13)	6.6(3)	PXD
Xia et al. (1998)	36.7	–	BS
	39.6	6.7	PXD
This study	35.8(9)	8.9(4)	BS

Notes: SW = Shock wave compression; PXD = Powder X-ray diffraction; PND = Powder neutron diffraction; SCXD = Single crystal X-ray diffraction; BS = Brillouin scattering.
* Fixed value.

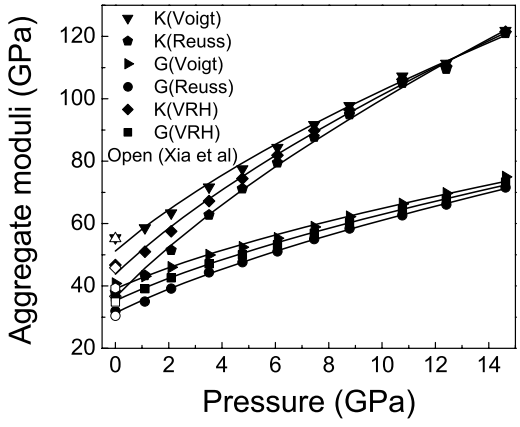

FIGURE 5. Brucite aggregate adiabatic bulk moduli K_S and G (filled symbols) and fits (lines) using Eulerian finite strain equations; open symbols are from Xia et al. 1998.

bounds, the aggregate σ value of brucite varies from 0.17(2) at 1 bar to 0.26(1) at 14.6 GPa. Finally, the elastic properties of brucite are also remarkable for the very high values of pressure derivatives in this system. The VRH average pressure derivative of the bulk modulus (K'_{VRH} = 6.8) is much larger than the typical value of 4. In some cases, it has been found that materials with high K' values are more appropriately fit with a higher order equation of state (Webb and Jackson 1993). In the case of brucite, only marginal improvement of the fit results from the use of 4th order finite strain equations for K and G, and the inclusion of an additional term is not justified. The pressure derivative of the shear modulus [$G' = \partial G/\partial P$ = 3.4(1) for Hill average, 4.3(1) for Reuss bound] for brucite is remarkably large. There are very few reported measurements of $G' \geq 2.5$ for minerals (e.g., Hofmeister and Mao 2003; Isaak 2001). Some of these reports appear to be of questionable quality, whereas for one material ($BaTiO_3$), the high G' value is clearly associated with recovery of the modulus immediately following a soft mode phase transition (Fischer et al. 1993). Neglecting such cases, brucite has the highest shear modulus pressure derivative yet reported in any mineral.

Volume compression behavior

An isothermal compression curve for brucite was constructed from our Brillouin measurements using the Reuss bound on the isothermal bulk modulus and its pressure derivative following the adiabatic to isothermal conversion discussed above (Table 5). Our compression curve (solid line) and its extrapolation to higher pressures (dotted line) are in very good agreement with selected previous static X-ray and neutron diffraction studies (Fig. 6). In contrast, there is a large range of reported K_{T0} and K'_{T0} values from previous studies (Table 6). The K_{T0} values of Fei and Mao (1993) and Parise et al. (1994) are higher and they are close to our Voigt bound values. While the K_{T0} values by other researchers (Catti et al. 1995; Duffy et al. 1995a; Nagai et al. 2000; Fukui et al. 2003a) are close to the Hill average of the Reuss-Voigt bound. These discrepancies could in part reflect differences in the strain state achieved in previous studies depending on experimental conditions and pressure medium used. However, it is expected that static compression results should be close to the Reuss bound. Many previous studies were conducted under non-hydrostatic conditions either with a solid or no pressure medium (e.g., Catti et al. 1995; Nagai et al. 2000; Fukui et al. 2003a), and it is well known that even small amounts of deviatoric stress can lead to an overestimate of the bulk modulus (Duffy et al. 1999). Our Reuss bound on K_{T0} is in very good agreement with a previous report using the Brillouin method at room pressure. In the present study, a 4:1 methanol-ethanol mixture was used as pressure transmitting medium. The sample remains under hydrostatic condition up to 12 GPa. The determination of the bulk modulus and its pressure derivative from static compression relies on fits to the slope of the measured P-V curve, and hence is less direct than Brillouin measurements. As a result, static compression also suffers from a well-known trade-off between fit values for K_{T0} and K'_{T0} (Bass et al. 1981). Furthermore, if measurements are restricted to purely hydrostatic conditions, the compression range is limited making it difficult to reliably constrain the bulk modulus. On the other hand, data that cover a broad pressure range are subjected to variable degrees of non-hydrostatic stress depending on the nature and amount of the pressure transmitting medium. The good agreement in Figure 6 between our calculated volumes and direct measurement indicate that despite large variance in reported bulk moduli and pressure derivatives, static compression data on brucite are generally in very good agreement with each other and with the present Brillouin results.

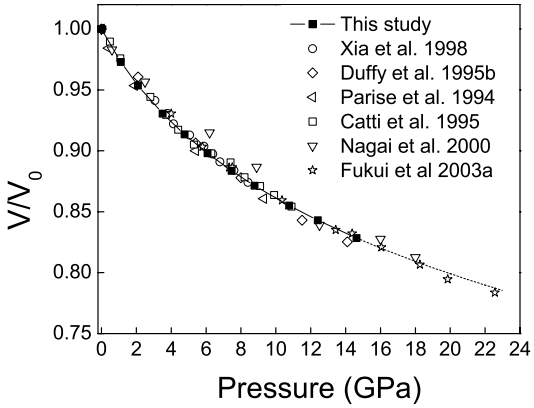

FIGURE 6. Isothermal compression curve of brucite calculated from the present study (solid line) and its extrapolation to higher pressures (dotted line). Previous compression studies are plotted for comparison.

Elastic anisotropy and the structure of brucite at high pressures

The elastic constants of brucite exhibit striking anisotropy at ambient pressures (Table 3, Fig. 4). The elastic constants C_{11} and C_{33} relate compressional stress to compressional strain along the a- and c-directions, respectively. At ambient pressure, C_{11} is 3.2(1) times greater than C_{33}, which reflects the large interlayer thickness and weak bonding along the c direction. C_{33} increases with pressure much more rapidly than C_{11} such that at 14.6(5) GPa the ratio of C_{11}/C_{33} has been reduced to 1.20(1). The strong anisotropy is also reflected in large differences between off-diagonal elastic constants C_{12} and C_{13}. C_{12} is about four times greater than C_{13} at room pressure. C_{13} increased by 513% in contrast to an increase of 65% for C_{12} over the examined pressure range, reducing the C_{13}/C_{12} ratio to 1.05(5). The shear anisotropy in trigonal crystals is given by the ratio of elastic constants $C_{66} = (C_{11} - C_{12})/2$ and C_{44} where C_{44} is the elastic modulus corresponding to shear waves propagating along the c axis and C_{66} is the elastic modulus corresponding to a shear wave propagating in the Y-direction in the basal plane (normal to Bravais a_1 axis) and polarized in the X-direction (parallel to Bravais a_1 axis). The shear anisotropy (C_{66}/C_{44}) decreased from 2.6(1) at room pressure to 1.3(1) upon compression to 12 GPa, where C_{66} is given by $(C_{11} - C_{12})/2$. Figure 7 shows the P-wave velocity data within the meridian plane at different pressures. The P-wave velocity increases by 75% along the c-axis direction in comparison with an increase of 10% along the a axis upon compression to 12.4 GPa.

The compression of brucite to modest pressures up to 15 GPa is thus sufficient to dramatically reduce the anisotropy ratios of pairs of related elastic constants. This pressure range corresponds to a region where a strong decrease in the crystallographic c/a

ratio is observed in X-ray and neutron diffraction experiments and theoretical calculations (Fei and Mao 1993; Catti et al. 1995; Duffy et al. 1995b; Nagai et al. 2000; Mookherjee and Stixrude 2005). Structure refinements and theory also indicate that over this pressure range the interlayer spacing along *c* decreases markedly whereas the octahedral layer thickness is mainly unchanged (Nagai et al. 2000; Mookherjee and Stixrude 2005). At ~12 GPa, the interlayer and octahedral layers achieve nearly the same thickness (Nagai et al. 2000; Mookherjee and Stixrude 2005). At higher pressures, the *c*/*a* ratio exhibits little further change with pressure and possibly even undergoes a slight increase with compression. The large increases of C_{33}, C_{13}, and C_{44} with compression therefore reflect a pronounced stiffening of the structure as the interlayer distance is reduced and there is a corresponding strong increase in interlayer bonding. At pressures above ~12 GPa, the compressibility of brucite in the *c* direction mainly reflects compression of the octahedral layer and the corresponding elastic constants (C_{33}, C_{13}, C_{44}) display shallower slopes compared with low-pressure behavior.

The value of C_{14} gives a measure of the anisotropy of the basal plane normal to the threefold axis. At ambient pressure, brucite is not resolvably different from the condition for transverse isotropy ($C_{14} = 0$). Basal plane anisotropy increases weakly with pressure (cf. Fig. 3). At the highest pressure, the maximum basal plane deviations from the values of C_{11}, C_{66}, and C_{44} are 0.5, 10, and 2%, respectively, indicating that longitudinal anisotropy in the basal plane remains small, but shear anisotropy becomes more appreciable.

The linear compressibility, β, of a crystal is the relative decrease in length when the crystal is subjected to hydrostatic pressure, and is defined for trigonal crystals by (Nye 1985):

$$\beta = (S_{11} + S_{12} + S_{13}) - (S_{11} + S_{12} - S_{13} - S_{33})n_3^2 \quad (4)$$

where n_3 is the direction cosine with the *c* axis, and the elastic compliances S_{ij} are converted to isothermal conditions. Figure 8 shows the linear compressibility curves for the meridian plane at various pressures. Figure 9 compares the pressure dependencies of linear compressibility along *c* and *a* axis derived from the present study together with data from a previous X-ray diffraction experiment (Xia et al. 1998). The linear compressibility along the *c* axis experienced a remarkable change in comparison with a moderate change for the direction along the *a* axis. The compression anisotropy is the ratio of the linear compressibility along the *c* and *a* axes (Chung and Buessem 1972). This quantity decreased from 4.7 to 1.3 over the examined pressure range. The compressibilities along the *a*-axis and *c*-axis directions are comparable at pressures above 14 GPa. Our high-pressure Brillouin results are in excellent agreement with independent static compression data.

Some previous studies have reported step changes in the *c*/*a* ratio at various pressures between 4 and 12 GPa (Fei and Mao et al. 1993; Catti et al. 1995; Nagai et al. 2000), while others have not observed such changes (Duffy et al. 1995b; Mookherjee and Stixrude 2005). Although no new diffraction peaks are observed, some new bands in the Raman spectrum associated with a Fermi resonance were also reported at 4 GPa in brucite (Duffy et al. 1995a). Parise et al. (1994) have shown that the hydrogen positions in brucite do not coincide with the threefold symmetry axis along *c* at high pressures but are split along three off-axis sites. Compression of brucite may therefore result in structural changes involving abrupt or continuous movement of hydrogen positions or changes in the degree of static or dynamic disorder (e.g., Mookherjee and Stixrude 2005). Increased H-H repulsion as the octahedral layers are compressed is thought to be a major driving force for structural evolution (Parise et al. 1994; Raugei et al. 1999; Mookherjee and Stixrude 2005). In this study, we observe that the C_{ij} values and hence axial compressibilities vary smoothly with pressure without any distinct discontinuities through the region of *c*/*a* changes and increasing hydrogen repulsion. The observed discontinuities in *c*/*a* may be related to uncertainties in diffraction data or variations in deviatoric stress as they are observed at different pressures and in some studies only. The elasticity data indicate that the increased interlayer interactions and hydrogen repulsion produce continuous variation in the mechanical response rather than any abrupt discontinuities.

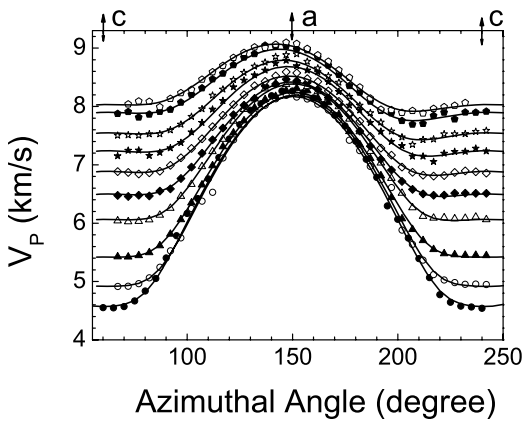

FIGURE 7. Quasi-longitudinal velocity data (symbols) and their fits for the meridian plane at pressures of 1 bar, 1.1, 2.1, 3.5, 4.8, 6.1, 7.5, 8.8, 10.8, 12.4, and 14.6 GPa, respectively, from bottom to top.

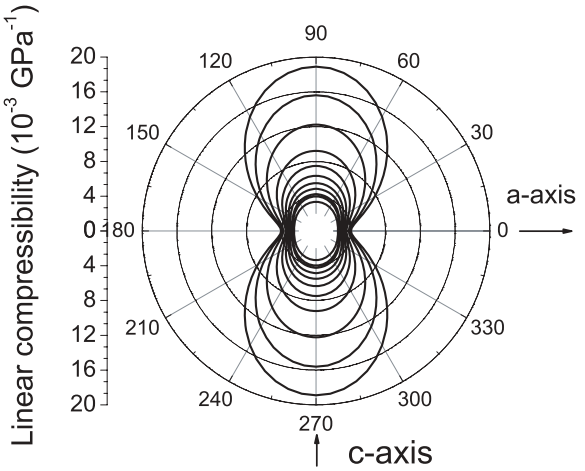

FIGURE 8. Anisotropy of linear compressibility curves in the meridian plane at pressures of 1 bar, 1.1, 2.1, 3.5, 4.8, 6.1, 7.5, 8.8, 10.8, 12.4, and 14.6 GPa, respectively, from outer to inner curves.

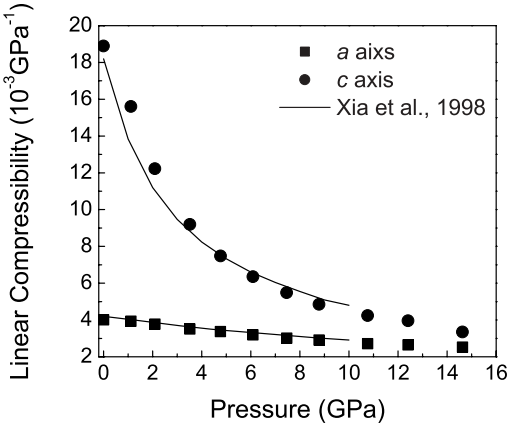

FIGURE 9. The calculated linear compressibilities of brucite as a function of pressure; symbols are from this study, and lines are from Xia et al. (1998).

Stability of brucite and comparison with portlandite

While the decomposition of brucite at relatively low pressures and high temperatures (e.g., Irving et al. 1977; Johnson and Walker 1993; Fukui et al. 2005) is well studied, it appears that brucite remains stable at high pressures (>80 GPa) to at least modest (600 K) temperatures (Duffy et al. 1991; Fei and Mao 1993). On the other hand, the isomorph portlandite, $Ca(OH)_2$, undergoes pressure-induced amorphization at 11 GPa (Meade and Jeanloz 1990) and transforms to a new polymorph at 7 GPa and 600 K (Kunz et al. 1996). The elastic moduli of portlandite, $Ca(OH)_2$, have also been reported at ambient pressure both by Brillouin experiment (Holuj et al. 1985) and calculated using density functional theory (DFT) (Laugesen 2005). The results from DFT calculations are similar to experiment except that C_{13} is found to be four times smaller than the experimental value, and this is more consistent with relative values of C_{ij} observed for brucite. The aggregate bulk modulus from the calculations is 26.6 GPa for the Reuss bound and 31.5 GPa for the VRH average. The bulk modulus obtained from static compression at high pressure is 33–38 GPa (Meade and Jeanloz 1990; Pavese et al. 1997; Fukui et al. 2003b). In general, the individual elastic moduli of portlandite are lower than brucite values and both exhibit strong elastic anisotropy. The anisotropy of longitudinal (C_{11}/C_{33}) and off-diagonal (C_{12}/C_{13}) moduli are similar in brucite and portlandite, but portlandite shows greater shear anisotropy (C_{66}/C_{44} = 3.2–4.3) compared with brucite (C_{66}/C_{44} = 2.6).

The Born stability criteria can be used to investigate the mechanical stability of brucite and portlandite. The stability criteria require that the elastic constant tensor be positive definite and for a trigonal crystal are (Fedorov 1958; Binggeli et al. 1994; Gregoryanz et al. 2000):

$$\begin{aligned} B_1 &= C_{11} - |C_{12}| > 0, \\ B_2 &= (C_{11} + C_{12})C_{33} - 2C_{13}^2 > 0, \\ B_3 &= (C_{11} - C_{12})C_{44} - 2C_{14}^2 > 0. \end{aligned} \quad (5)$$

For brucite, all three stability criteria are satisfied. The magnitudes of B_1, B_2, and B_3 increase over the experimental pressure range, supporting the continued mechanical stability of the phase to high pressures. For portlandite, the stability criteria are also satisfied when using theoretical elastic constants but their values are lower than for brucite. The value of B_3 for portlandite is only 20% of the value for brucite. High-pressure elastic constants for $Ca(OH)_2$ are needed to evaluate the mechanical stability as pressure-induced amorphization is approached.

Implications for the mantle

Layered hydrous minerals are potentially important geological constituents of the upper mantle. The contrasting elastic properties between related hydrous and anhydrous minerals (e.g., forsterite and serpentine) can be a useful diagnostic tool in interpreting seismic observations of the mantle. At ambient pressure, the elastic wave velocities of hydrous layered minerals are generally characterized by low average values and high anisotropy compared with other minerals. Our results for brucite show that the degree of anisotropy can be reduced rapidly upon application of pressure. Furthermore, the aggregate velocity contrast is also reduced. At ambient pressure, aggregate compressional, bulk, and shear wave velocities in brucite are about 50% lower than those in the anhydrous oxide periclase (MgO) (Sinogeikin and Bass 2000). However, extrapolating our measurements to 20 GPa indicates that velocity contrast is reduced to about 13% for bulk sound waves and 26% for shear velocity. At 1 Mbar, the bulk wave velocity of brucite is within 3% of periclase values consistent with earlier inferences from shock compression data (Duffy et al. 1991) whereas the shear velocity contrast remains larger (17%). If applicable to other hydrous minerals including silicates, these results suggest that hydrous minerals will become increasingly difficult to detect with depth but that shear velocity contrast may be greater than that of other wave speeds.

ACKNOWLEDGMENTS

We thank J. Hu for assistance with X-ray diffraction measurements and Jim Eckert (Yale) for performing the microprobe analysis. This work was supported by the NSF and the Carnegie-DOE alliance center. Use of the National Synchrotron Light Source, Brookhaven National Laboratory, was supported by the U.S. Department of Energy, Office of Science, Office of Basic Energy Sciences, under contract no. DE-AC02-98CH10886.

REFERENCES CITED

Bass, J.D., Liebermann, R.C., Weidner, D.J., and Finch, S.J. (1981) Elastic properties from acoustic and volume compression experiments. Physics of the Earth and Planetary Interiors, 25, 140–158.

Berman, R.G. and Brown, T.H. (1985) Heat capacity of minerals in the system Na_2O-K_2O-CaO-MgO-FeO-Fe_2O_3-Al_2O_3-SiO_2-TiO_2-H_2O-CO_2: representation, estimation, and high-temperature extrapolation. Contributions to Mineralogy and Petrology, 89, 168–183.

Binggeli, N., Keskar, N.R., and Chelikowsky, J.R. (1994) Pressure-induced amorphization, elastic instability, and soft modes in α-quartz. Physical Review B, 49, 3075–3081.

Birch, F. (1978) Finite strain isotherm and velocities for single-crystal and polycrystalline NaCl at high pressures and 300 K. Journal of Geophysical Research, 83, 1257–1264.

Catti, M., Ferraris, G., Hull, S., and Parise, A. (1995) Static compression and H disorder in $Mg(OH)_2$ to 11 GPa: A powder neutron diffraction study. Physics and Chemistry of Minerals, 22, 200–206.

Chung, D.H. and Buessem, W.R. (1968) The elastic anisotropy of crystals. In F.W. Vahldiek and S.A. Mersol, Eds., Anisotropy in Single Crystal Refractory Compounds, 2, p. 217–245. Plenum, New York.

Duffy, T.S., Ahrens, T.J., and Lange, M.A. (1991) The shock-wave equation of state of brucite, $Mg(OH)_2$. Journal of Geophysical Research, 96, 14319–14330.

Duffy, T.S., Meade, C., Fei, Y.W., Mao, H.K., and Hemley, R.J. (1995a) High-pressure phase-transition in brucite, $Mg(OH)_2$. American Mineralogist, 80, 222–230.

Duffy, T.S., Shu, J., Mao, H.K., and Hemley, R.J. (1995b) Single-crystal X-ray diffraction of brucite to 14 GPa. Physics and Chemistry of Minerals, 22,

277–281.
Duffy, T.S., Shen, G., Heinz, D.L., Shu, J., Ma, Y., Hemley, R.J., and Mao, H.K. (1999) Lattice strains in gold and rhenium to 37 GPa. Physical Review B, 60, 15063–15073.
Every, A.G. (1980) General closed-form expressions for acoustic waves in elastically anisotropic solids. Physical Review B, 22, 1746–1760.
Fedorov, F.I. (1958) Theory of elastic waves in crystals. Plenum Press, New York.
Fei, Y. and Mao, H.K. (1993) Static compression of $Mg(OH)_2$ to 78 GPa at high temperature and constraints on the equation of state of fluid H_2O. Journal of Geophysical Research, 98, 11875–11884.
Fischer, G.J., Wang, Z.C., and Karato, S. (1993) Elasticity of $CaTiO_3$, $SrTiO_3$, and $BaTiO_3$ perovskites up to 3.0 GPa—the effect of crystallographic structure. Physics and Chemistry of Minerals, 20, 97–103.
Fukui, H., Ohtaka, O., Suzuki, T., and Funakoshi, F. (2003a) Thermal expansion of $Mg(OH)_2$ brucite under high pressure and pressure dependence of entropy. Physics and Chemistry of Minerals, 30, 511–516.
Fukui, H., Ohtaka, O., Fujisawa, T., Kunisada, T., Suzuki, T., and Kikegawa, T. (2003b) Thermo-elastic property of $Ca(OH)_2$ portlandite. High Pressure Research, 23, 55–61.
Fukui, H., Inoue, T., Yasui, T., Katsura, T., Funakoshi, K., and Ohtaka, O. (2005) Decomposition of brucite up to 20 GPa: evidence for high MgO-solubility in the liquid phase. European Journal of Mineralogy, 17, 261–267.
Gregoryanz, E., Hemley, R.J., Mao, H.K., and Gillet, P. (2000) High-pressure elasticity of α-quartz: instability and ferroelastic transition. Physical Review Letters, 84, 3117–3120.
Hofmeister, A.M. and Mao, H.K. (2003) Pressure derivatives of shear and bulk moduli from the thermal Gruneisen parameter and volume-pressure data. Geochimica et Cosmochimica Acta, 67, 1207–1227.
Holuj, F., Drozdowski, M., and Czajkowski, M. (1985) Brillouin spectrum of $Ca(OH)_2$. Solid State Communications, 56, 1019–1021.
Hostetler, P.B., Coleman, R.G., and Mumpton, F.A. (1966) Brucite in Alpine serpentinites. American Mineralogist, 51, 75–98.
Irving, A.J., Huang, W.L., and Wyllie, P.J. (1977) Phase relations of portlandite, $Ca(OH)_2$ and brucite, $Mg(OH)_2$ to 33 kilobars. American Journal of Science, 277, 313–321.
Isaak, D.G. (2001) Elastic properties of minerals and planetary objects. In M. Levy, J. Bass, and R. Stern, Eds., Handbook of Elastic Properties of Solids, Liquids, and Gases: Volume III: Elastic Properties of Solids: Biological and Organic Material, Earth and Marine Sciences, p. 325–376. Academic Press, San Diego.
Jiang, F., Speziale, S., Shieh, S.R., and Duffy, T.S. (2004a) Single-crystal elasticity of andradite garnet to 11 GPa. Journal of Physics: Condensed Matter, 16, S1041–S1052.
Jiang, F., Speziale, S., and Duffy, T.S. (2004b) Single-crystal elasticity of grossular- and almandine-rich garnets to 11 GPa by Brillouin scattering. Journal of Geophysical Research, 109, B10210.
Johnson, M.C. and Walker, D. (1993) Brucite [$Mg(OH)_2$] dehydration and the molar volume of H_2O to 15 GPa. American Mineralogist, 78, 271–284.
Kruger, M.B., Williams, Q., and Jeanloz, R. (1989) Vibrational-spectra of $Mg(OH)_2$ and $Ca(OH)_2$ under pressure. Journal of Chemical Physics, 91, 5910–5915.
Kunz, M., Leinenweber, K., Parise, J.B., Wu, T.C., Bassett, W.A., Brister, K., Weidner, D.J., Vaughan, M.T., and Wang, Y. (1996) The baddeleyite-type high-pressure phase of $Ca(OH)_2$. High Pressure Research, 14, 311–319.
Laugesen, J.L. (2005) Density functional calculations of elastic properties of portlandite, $Ca(OH)_2$. Cement and Concrete Research, 35, 199–202.
Mao, H.K., Xu, J., and Bell, P.M. (1986) Calibration of the ruby pressure gauge to 800 kbar under quasi-hydrostatic conditions. Journal of Geophysical Research, 91, 4673–4676.
Meade, C. and Jeanloz, R. (1990) Static compression of $Ca(OH)_2$ at room-temperature observations of amorphization and equation of state measurements to 10.7 GPa. Geophysical Research Letters, 17, 1157–1160.
Mirwald, P.W. (2005) The fine-structure of the dehydration boundary of brucite $Mg(OH)_2$ up to 3.5 GPa—indication of anomalous *PVT* behavior of supercritical H_2O. European Journal of Mineralogy, 17, 537–542.
Mookherjee, M. and Stixrude, L. (2005) High-pressure proton disorder in brucite. American Mineralogist, 91, 127–134.
Nagai, T., Hattori, T., and Yamanaka, T. (2000) Compression mechanism of brucite: An investigation by structural refinement under pressure. American Mineralogist, 85, 760–764.
Nye, J.F. (1985) Physical Properties of Crystals: Their Representation by Tensors and Matrices, p. 146. Clarendon Press, Oxford.
Parise, J.B., Leinenweber, K., Weidner, D.J., Tan, K., and Von Dreele, R.B. (1994) Pressure-induced H bonding: neutron diffraction study of brucite, $Mg(OH)_2$, to 9.3 GPa. American Mineralogist, 79, 193–196.
Pavese, A., Catti, M., and Ferraris, G. (1997) *P-V* equation of state of portlandite, $Ca(OH)_2$, from powder neutron diffraction data. Physics and Chemistry of Minerals, 24, 85–89.
Peacock, S.M. and Hyndman, R.D. (1999) Hydrous minerals in the mantle wedge and the maximum depth of subduction thrust earthquakes. Geophysical Research Letters, 26, 2517–2520.
Raugei, S., Silvestrelli, P.L., and Parrinello, M. (1999) Pressure-induced frustration and disorder in $Mg(OH)_2$ and $Ca(OH)_2$. Physical Review Letters, 83, 2222–2225.
Redfern, S. and Wood, B.J. (1992) Thermal-expansion of brucite $Mg(OH)_2$. American Mineralogist, 77, 1129–1132.
Shieh, S.R. and Duffy, T.S. (2002) Raman spectroscopy of $Co(OH)_2$ at high pressures: Implications for amorphization and hydrogen repulsion. Physical Review B, 66, 134301.
Shim, S.H., Rekhi, S., Martin, M.C., and Jeanloz, R. (2006) Vibrational spectroscopy and X-ray diffraction of $Cd(OH)_2$ to 28 GPa at 300 K. Physical Review B, 74, 024107.
Shimizu, H. (2004) High-pressure in situ Brillouin spectroscopy in a diamond-anvil cell. High Pressure Research, 24, 491–498.
Shinoda, K., Yamakata, M., Nanba, T., Kimura, H., Moriwaki, T., Kondo, Y., Kawamoto, T., Niimi, N., Miyoshi, N., and Aikawa, N. (2002) High-pressure phase transition and behavior of protons in brucite $Mg(OH)_2$: a high-pressure-temperature study using IR synchrotron radiation. Physics and Chemistry of Minerals, 29, 396–402.
Sinogeikin, S.V. and Bass, J. D. (2000) Single-crystal elasticity of pyrope and MgO to 20 GPa by Brillouin scattering in the diamond cell. Physics of the Earth and Planetary Interior, 120, 43–62.
Speziale, S. and Duffy, T.S. (2002) Single-crystal elastic constants of fluorite (CaF_2) to 9.3 GPa. Physics and Chemistry of Minerals, 29, 465–472.
Speziale, S., Jeanloz, R., Milner, A., Pasternak, M.P., and Zaug, J.M. (2005) Vibrational spectroscopy of $Fe(OH)_2$ at high pressure: Behavior of the O-H bond. Physical Review B, 71, 184106.
Watt J.P., Davies, G.F., and O'Connell, R.J. (1976) The elastic properties of composite materials. Review of Geophysics and Space Physics, 14, 541–563.
Webb, S.L. and Jackson, I. (1993) The pressure-dependence of the elastic-moduli of single-crystal ortho-pyroxene $Mg_{0.8}Fe_{0.2}SiO_3$. European Journal of Mineralogy, 5, 1111–1119.
Whitfield, C.H., Brody, E.M., and Bassett, W.A. (1976) Elastic moduli of NaCl by Brillouin scattering at high pressure in a diamond cell. Review of Scientific Instruments, 47, 942–947.
Xia, X., Weidner, D.J., and Zhao, H. (1998) Equation of state of brucite: Single-crystal Brillouin spectroscopy study and polycrystalline pressure-volume-temperature measurement. American Mineralogist, 83, 68–74.

MANUSCRIPT RECEIVED JANUARY 19, 2006
MANUSCRIPT ACCEPTED JUNE 26, 2006
MANUSCRIPT HANDLED BY PRZEMYSLAW DERA